ACS Biomaterials SCIENCE & ENGINEERING

pubs.acs.org/journal/abseba

Article

Ultrasonic Formation of Fe_3O_4-Reduced Graphene Oxide–Salicylic Acid Nanoparticles with Switchable Antioxidant Function

Lubov Mikhnavets, Viktar Abashkin, Hanna Khamitsevich, Dzmitry Shcharbin, Aliaksandr Burko, Nina Krekoten, and Darya Radziuk*

Cite This: https://doi.org/10.1021/acsbiomaterials.1c01603

Read Online

ACCESS | Metrics & More | Article Recommendations | Supporting Information

ABSTRACT: We demonstrate a single-step ultrasonic in situ complexation of salicylic acid during the growth of Fe_3O_4-reduced graphene oxide nanoparticles (~10 nm) to improve the antioxidant and antiproliferative effects of pristine drug molecules. These nanoparticles have a precisely defined electronic molecular structure with salicylic acid ligands specifically complexed to Fe(III)/Fe(II) sites, four orders of magnitude larger electric surface potential, and enzymatic activity modulated by ascorbic acid molecules. The diminishing efficiency of hydroxyl radicals by Fe_3O_4-rGO-SA nanoparticles is tenfold higher than that by pristine salicylic acid in the electro-Fenton process. The H^+ production of these nanoparticles can be switched by the interaction with ascorbic acid ligands and cause the redox deactivation of iron or enhanced antioxidation, where rGO plays an important role in enhanced charge transfer catalysis. Fe_3O_4-rGO-SA nanoparticles are nontoxic to erythrocytes, i.e., human peripheral blood mononuclear cells, and surpassingly inhibit the growth of three cancer cell lines, HeLa, HepG2, and HT29, with respect to pristine salicylic acid molecules.

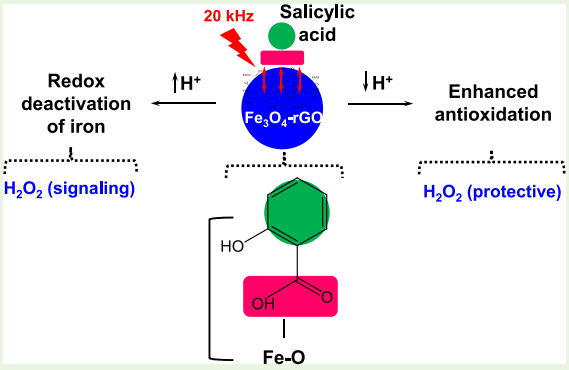

KEYWORDS: *iron oxide, graphene, NSAID, biocatalyst, inflammation, cancer*

1. INTRODUCTION

Salicylic acid (SA)-based drugs are widely used in type II diabetes, Alzheimer's disease, rheumatism, and cancer.[1,2] SA exhibits beneficial antioxidant properties via direct interaction with enzymes or by controlling their de novo synthesis.[3] The antioxidant properties of SA are determined in the reduction of tissue damage caused by hypoxia/reoxygenation, where SA diminishes hydroxyl radicals due to specific binding to protein and modifying its function. SA can inhibit the mitochondrial damage and preserve the ascorbate depletion due to ischemia/reperfusion in the heart.[4] The physiological antioxidant action of SA is observed in the decrease of flux of hydroxyl radicals through chelation, which causes a redox deactivation mechanism of iron Fenton reaction centers.[5] SA is considered a better in vivo hydroxyl radical scavenger than ascorbic acid (AA) in its ionized form or cysteine because of its site-specific location, iron-binding ability, and high reaction rate ($6–10 \times 10^9$ M^{-1} s^{-1}).[6] Therefore, the iron–salicylate complex does not have the thermodynamic driving force to act as an effective Fenton reagent necessary for the production of damaging oxygen-containing radicals. Such salicylate complexes act by redox deactivation of iron and may mimic a superoxide dismutation (SOD), indicating another antioxidant property of SA. It was shown that the salicylate–iron complex can inhibit the xanthine oxidase properties and stimulate the formation of H_2O_2 during the dismutation reaction.[7] In addition, salicylate–iron can simultaneously reduce Fe(III) of the complex to Fe(II), generating hydroxyl radicals during dismutation, which is indicative of the pro-oxidant action. SA (a metabolite of aspirin) causes severe side effects (stomach ulcer formation, bleeding, nausea, vomiting, etc.). Therefore, new methods are needed to control the SA structure in salicylate complexes aiming at improved antioxidant and enzymatic efficiency modulation.

Metallodrugs are effective in clinical therapy of oncological tumors[8] according to the mechanism of their action.[9] The efficiency of metallodrugs is explained by metal ions or atom activation of their versatile structure, resulting in rich and multifaceted coordination functions.[10] To date, activation of SA is accounted for complexation with silver for improved wound healing[11] and human breast cancer therapy,[12] with iridium for potent tumor growth inhibition,[13] with copper for a

Received: January 10, 2022
Accepted: February 17, 2022

higher antitumor efficacy by the proposed ROS-mediated mitochondrial pathway[14] with respect to pristine SA.

Metal complexes can enhance the lethality of irradiated HeLa cells with a higher efficiency when ascorbate is co-administered with Mn(III) species.[15] A high proportion of cancer cell lines is sensitive to H_2O_2 and produces elevated amounts of superoxide via NADPH oxidase complexes or dysfunctional mitochondria. This superoxide can generate a deadly hydroxyl radical (Haber−Weiss reaction) via a transition metal-catalyzed transfer of an electron to H_2O_2 produced by ascorbate.[16] H_2O_2 formation depends on ascorbate concentration and incubation time and exhibits a linear relationship with ascorbate radical formation,[17] resulting in killing malignant but not benign cells. H_2O_2 decomposition can be modulated by AA adsorbed on core−shell Fe/Fe_2O_3 nanowires, resulting in the production of hydroxyl radicals in the Fenton process.[18] The formed iron−ascorbate complex stabilizes ferrous ions with a steady concentration to maintain the Fe(III)/Fe(II) cycle, acting as a reducing and complexing reagent during the $AA/Fe@Fe_2O_3/H_2O_2$ Fenton process, enabling the reuse of $Fe@Fe_2O_3$ nanowires. However, AA can be degraded in the $AA/Fe@Fe_2O_3$ system, but oxidized AA can be reduced back or oxidized further.[19] AA can react directly with hydroxyl radicals, superoxide ions, and molecular oxygen and reduce H_2O_2 via the ascorbate−glutathione pathway, mitigating oxidative stress.[20]

An ancillary protective mechanism of AA in many tissues can be explained by its reaction with $O_2^{\bullet-}$: ascorbate $+2H^+ + 2O_2^{\bullet-} \rightarrow 2H_2O_2$ + dehydroascorbate. Autooxidation of ascorbate at physiological pH can be completely inhibited by superoxide dismutase (SOD), suggesting that $O_2^{\bullet-}$ is produced during this reaction. AA causes DNA damage, increases the levels of catalase, SOD, and ER stress-related proteins, and enhances the susceptibility of HeLa cells to anticancer drugs[21] but with different sensitivities, which is not understood yet.[22] Only actively proliferating cells including metastatic invasion are affected by AA treatment, and an increased ascorbate concentration did not improve the cytotoxicity, which cannot be explained why. So far, the antiproliferative effects have been ascribed to the antioxidant properties of AA. Treatment with increasing doses of AA is understood by the induction of a specific downregulation of a selected set of genes. AA enhances the passive membrane permeability but with a lower efficiency than SA, which inhibits the growth of HeLa cells via caspase 3 activation[23] and inhibition of nuclear factor kappa B (NFκB) transcriptional activation.[24] In contrast to ascorbate, SA increases ROS production via its action by the carboxylic group as shown in the HT-29 human colorectal carcinoma cell line[25] and can sensitize these cells to H_2O_2 in apoptosis induced by TNF-K or a Fas ligating antibody.[26]

So far, the complexation of SA with iron(II) or iron(III) is mainly introduced by the study of the electronic structure of iron−salicylates and identification of chemical coordination groups of biological importance.[27] The iron(II)/iron(III) switch is essential not only for enzymatic functions but also for the formation of highly reactive hydroxyl radicals.[28] However, such metal complexes undergo ligand substitution reactions at inorganic centers and their structure/function properties cannot be predicted in vivo.

Alternatively, the specific interaction of metal-based nanoparticle (NP) drugs with biological entities can be controlled by their size, shape, and structure. For example, superparamagnetic Fe_3O_4 NPs (<20 nm) can be safely applied as biocompatible, biodegradable, and non-toxic contrast agents in magnetic resonance imaging.[29] At present, the Food and Drug Administration approved ferumoxytol drug containing iron oxide NPs used for iron deficiency treatment and tumor retardation growth.[30] Moreover, oral tablet formulation of anticancer drug celecoxib includes Fe_2O_3 NPs and non-steroidal anti-inflammatory drug (NSAID) indomethacin−Fe_3O_4 NPs. However, the interaction of these drug molecules with ferric or ferrous oxide has not been determined and the catalytic properties of iron-activated drugs as nanoparticles have not been studied yet.

Up to now, Fe_3O_4 NPs have been designed with graphene oxide (GO), providing a platform of many functional groups: carboxylic (−COOH), hydroxyl (−OH), carbonyl (−C═O), and epoxide (−C−O−C). This strategy has been successfully applied to complexation of doxorubicin[31] or folic acid[32] with enhanced intracellular uptake and targeted imaging of oncological tumors. In these studies, Fe_3O_4 NPs are either grown or coated with GO that is loaded with anticancer drugs. Previously, we have introduced a new approach based on the ultrasonic complexation of pristine NSAIDs−ketorolac or aspirin with preformed Fe_3O_4 NPs grown on GO.[33,34] GO especially stands out here as it provides more binding sites for complexation with drugs and improves the electronic properties and stability of potential pharmaceutical compounds. As an advantage, ultrasound causes efficient complexation of drug molecules in NPs so that the structure of pharmaceutical organic ligands does not undergo severe damage and remain stable during the synthesis. So far, the effects of ultrasound have been determined in sonofragmentation of molecular[35] and ionic[36] crystals, sonocatalysis of iron carbonyls,[37] synthesis of iron colloids,[38] nanosized hollow hematite,[39] and functionalized graphenes.[40] In this context, the sonochemical effects of pristine or complexed NSAID NPs have not been defined yet.

2. EXPERIMENTAL SECTION

Chemicals, details about the synthesis of GO, preparation of colloidal aqueous solutions for fluorescence measurements, cell culture experiments, electrochemical measurements of NPs in the electro-Fenton process, and characterization are described in detail in the Supporting Information.

2.1. Synthesis of Fe_3O_4-rGO-SA Nanoparticles. A horn-type ultrasonic disperser N.4-20 (20 kHz, 400 W) designed by Cavitation Inc. (Republic of Belarus) was used for the ultrasonic synthesis of nanoparticles. Prior to the synthesis, 100 mg of GO was triply exfoliated in 20 mL of the aqueous solution consisting of DI water at pH 5.5 and isopropanol at a volume ratio of 3:1 by using ultrasound (10 W cm^{-2}) for 5 min in an ice-cooled vessel. The exfoliated GO was triply rinsed with DI water by centrifugation at 7.3*g* for 15 min and added with 10 mL of DI water (pH 5.5) followed by 3 min of sonication to obtain a homogeneous colloidal solution. An aqueous mixture of 362 mM $FeCl_3$ and 170 mM $FeCl_2$ was mechanically stirred in an Ar atmosphere for 15 min and then heated at 80 °C for 15 min. Next, the pre-treated GO (10 mL) colloidal solution was sonicated for 5 min in an air atmosphere. Soon after, this colloidal solution was dropwise added with 5 mL of 44% KOH while being mechanically stirred and heated continuously. Next, 6 mL of 44% KOH was dropwise added into the mixture until the black color appeared and heating at 80 °C continued for 30 min in an Ar atmosphere. Next, 29.1 mM SA aqueous solution was added, and the mixture was sonicated at 18 W cm^{-2} and stirred for 5 min in an Ar atmosphere. After synthesis, the colloidal solution obtained a dark black-brown color and its pH was 5. Then, this colloidal solution was cooled down to room temperature, triply rinsed with DI water (pH = 5.5) by centrifugation at 6.7*g* for 15 min, and air-dried at 100 °C to obtain a final powder. The formed solid product responded to an

https://doi.org/10.1021/acsbiomaterials.1c01603
ACS Biomater. Sci. Eng. XXXX, XXX, XXX−XXX

Scheme 1. Schematic Illustration Showing the Ultrasonically Formed Fe_3O_4-rGO-SA Nanoparticles (~10 nm) with Switchable Antioxidant Function Modulated by the Interaction with Pristine Ascorbic Acid for Controlled Inhibition of Cancer Cell Growth[a]

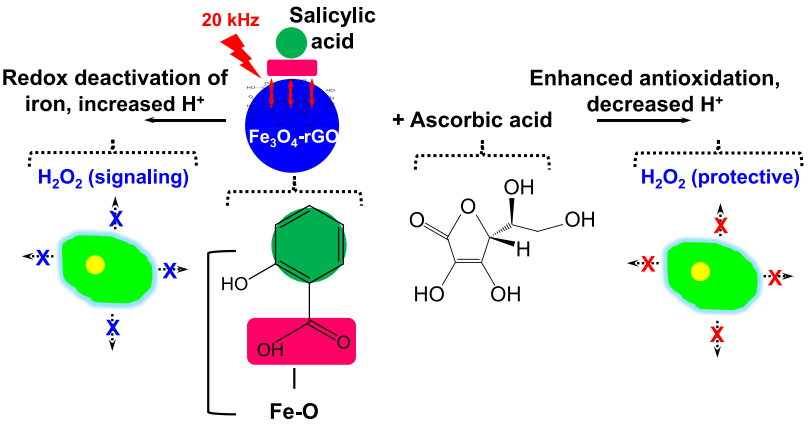

[a]Ultrasonic complexation of pristine salicylic acid (SA) ligands is derived from binding of a phenyl ring with a carboxylic group to Fe−O. Such an electronic structure of nanoparticles facilitates H^+ production in a redox deactivation of iron and inhibits proliferation via H_2O_2 signaling. Adsorption of ascorbic acid molecules on nanoparticles reduces H^+ production and enhances antioxidant function via H_2O_2 involving a protective mechanism.

external magnet. Then, 100 mg of this solid product was mixed with 29.1 mM SA aqueous mixture consisting of DI water and isopropanol at a volume ratio of 1:1 and ultrasonically treated at 18 W cm^{-2} (5 min) in an air atmosphere. The final product was triply rinsed with DI water by centrifugation (at 6.7*g*) for 15 min, filtered through a cellulose membrane filter (violet line, the pore size <1−2 μm), and air-dried at 100 °C. The control nanoparticles were prepared by using a similar procedure without GO or SA.

2.2. Theoretical Modeling of the Current Density and Potential Distribution of Nanoparticles. The current density pattern was calculated by using a Comsol Multiphysics software tool. In this calculation, the fundamental equation of the current conduction or charge conservation (eq 2) on the surface of nanoparticles is computed

$$\Delta\cdot(-\sigma\Delta V) = 0 \tag{2}$$

where σ is the electrical conductivity (S/m) and V is the electric potential (V).

In this model, we use the electrical conductivities of Fe_3O_4 nanoparticles with about 30 nm average diameter as 1×10^4 S/m, of Fe_3O_4-SA nanoparticles with ~15 nm diameter as 3×10^4 S/m, and of Fe_3O_4-rGO-SA as 3×10^2 S/m. The values of electric potential V are considered from the electrochemical measurements of CV curves with the peak magnitudes corresponding to the •OH evolution. The potential distribution is computed across the surface of nanoparticles varying their average diameter with the added current field flow as an arrow plot. The local magnitude of the electric current density (A/m^2) is computed by using the current conduction eq 3 (a coefficient form boundary PDE interface) with the diffusion coefficient

$$c = \sigma \times d \tag{3}$$

where d is the electrochemical shell thickness (nm).

Due to the symmetry of the nanosphere, only one cross section along the *yz* plane is modeled. In the model, we use the initial time derivative of the potential $\delta V/\delta t$ = 0.01 V/s, the conservative flux convection coefficient α (S/m) with x = 1, y = 1, and z = 1, convection coefficient β (S/m) with x = 1, y = 1, and z = 1, and the conservative flux source γ (A/m) with x = 1, y = 1, and z = 1. The model is illustrated in eq 4 as follows:

$$e_a\frac{\partial^2 V}{\partial t^2} + d_a\frac{\partial V}{\partial t} + \Delta\cdot(-c\Delta\cdot V - \alpha V + \gamma) + \beta\cdot\Delta V + \alpha V = f \tag{4}$$

where e_a is the mass coefficient (S^5A^2/m^4 kg, set to zero), d_a is the damping coefficient (F/m^2, set to 1), and f is the source term (A/m^2).

2.3. Theoretical Modeling of the H^+ Production in NPs (the Three-Electrode Surface System). This modeling is based on the fundamental computation of the electrochemical treatment of tumors with implication that the diseased tissue is treated with the direct current through the use of the metallic electrodes inserted inside the cellular environment.[41] We assume that when the tissue is electrolyzed, two competing reactions take place at the anode: oxygen evolution and chlorine production. The oxygen evolution reaction also produces H^+ ions, which lower the pH value close to the anode according to the following reactions:

$$2Cl^- = Cl_2 + 2e^- \text{ at the cathode} \tag{5}$$

$$2H_2O = 4H^+ + O_2 + 4e^- \text{ at the anode} \tag{6}$$

In this model, we apply the Nernst−Planck equation interface using a Comsol Multiphysics software tool to compute the concentration of H^+ ions developed close to the electrode surface in contact with the nanoparticles. We calculate the amount of H^+ ions at different concentrations of complexed SA molecules in NPs in an aqueous electrolyte solution of KCl before and after addition of ascorbic acid. At the electrode surface, the fluxes of H^+ and Cl^- ions are included in the electrochemical reactions, while the K^+ ionic species are considered inert in this model. In the model, the following equation (eq 7) is used for molar fluxes at the boundary for the reacting species

$$N_i\cdot n = \frac{\nu_{ij}J_j}{n_j\cdot F} \tag{7}$$

where N_i is the flux, ν_{ij} is the stoichiometric coefficient for the ionic species i in reaction j, and n_j is the number of electrons in reaction j.

The current density for the oxygen evolution reaction is calculated in the following equation (eq 8):

$$j_I = j_{I,0}\{e^{-F(V+E_{eq,I0})/2RT} - (P_{O2})^{1/4}C_{H+}e^{F(V+E_{eq,I})/2RT}\} \tag{8}$$

where $j_{I,0}$ is the exchange current density (A/m^2) and $E_{eq,I}$ is the standard electrode potential (V). The fluxes of H^+ ions at the electrode surface (N_H) are computed according to eq 8 using the input values n_I = 1 and $\nu_{H,I}$ = 1:

$$N_H\cdot n = \frac{j_I}{F} \tag{9}$$

https://doi.org/10.1021/acsbiomaterials.1c01603
ACS Biomater. Sci. Eng. XXXX, XXX, XXX−XXX

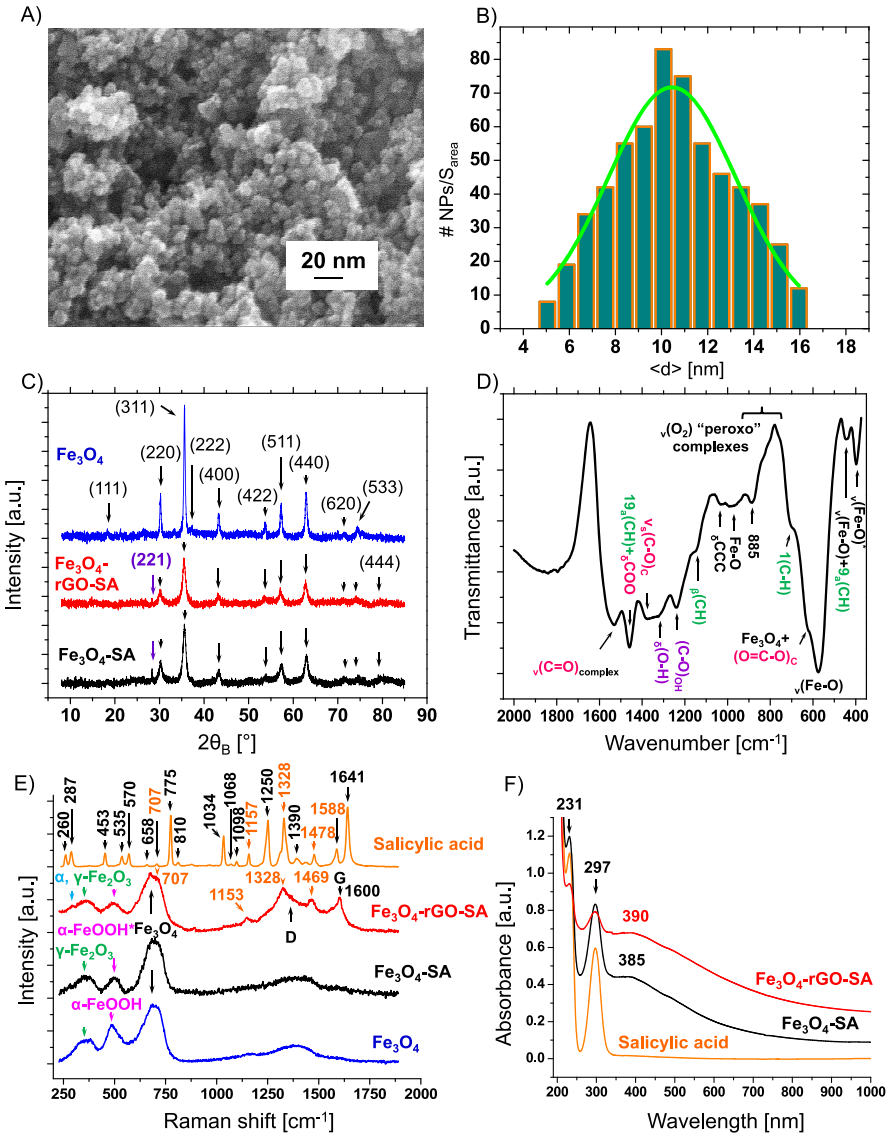

Figure 1. (A) Representative SEM image and (B) size distribution histogram (number of NPs per surface area versus the average size ⟨d⟩, nm) of synthesized Fe_3O_4-rGO-SA NPs are demonstrated. (C) X-ray diffraction patterns of Fe_3O_4-rGO-SA NPs in comparison with Fe_3O_4 and Fe_3O_4-SA are shown. (D) FT-IR transmittance spectrum of Fe_3O_4-rGO-SA NPs is demonstrated in the spectral region of 400−2000 cm^{-1}. (E) Raman (λ_{exc} = 633 nm) and (F) UV−Vis absorbance spectra of Fe_3O_4-rGO-SA NPs in comparison with Fe_3O_4-SA, Fe_3O_4, and free SA molecules in aqueous solutions (pH 5, T = 22 °C) are shown.

where n is the number of electrons, j_I is the exchange current density (A/m^2) in the reaction of oxygen evolution, and F is the Faraday's constant (c/mol).

In the model, we use the diffusion coefficients of H^+ (D_H) 9.31×10^{-9} m^2/s and of Cl^- (D_{Cl}) 2.03×10^{-9} m^2/s and the initial concentrations of KCl (C_{KCl}) 4.76 mol/L and of H^+ (C_H) = 1×10^{-7} mol/L. The primary anodic peak is assumed as the value for the $^{\bullet}OH$ production and the equilibrium potential reaction for oxygen evolution being 1.2 V. The proton concentration is computed in the domain at different time steps from 0 to 3600 s, considering that at high current densities, the concentration of produced protons is increased and it forms a front moving inward in the domain with a lower current density.

More details about the Raman and energy dispersive X-ray fluorescence (EDX) spectra of rGO, SEM analysis of Fe_3O_4-SA NPs, XRD analysis of Fe_3O_4-rGO-SA and Fe_3O_4-SA NPs, FTIR transmittance spectra of Fe_3O_4-rGO-SA NPs (2400−3800 cm^{-1}) and Fe_3O_4-SA NPs (400−3800 cm^{-1}), Raman and EDX spectra of NPs, UV−Vis absorption spectra of aqueous solutions of NPs, cyclic voltammograms of the electro-Fenton process with bare Fe_3O_4-SA NPs before and after stepwise addition of ascorbic acid aqueous solution, optical phase contrast images, and statistical diagrams of live HeLa, HepG2, and HT29 cancer cells with incubated NPs can be found in the Supporting Information.

3. RESULTS AND DISCUSSION

Distinct from existing studies, the main idea of this work is to demonstrate a single-step ultrasonic (20 kHz) complexation of pristine SA molecules in in situ formation of magnetite-reduced GO (rGO) and examine their enhanced structure/function properties (Scheme 1).

Ultrasonic complexation enhances the electronic molecular SA structure in Fe_3O_4-rGO-SA NPs through the binding of the phenyl ring with the carboxylic group to Fe−O to contract oxidation via redox deactivation of iron and H^+ production for enzymatic growth inhibition of HeLa, HepG2, and HT29 cancer cells. We also determine the crucial role of rGO in enhanced charge transfer catalysis and AA as a molecular

https://doi.org/10.1021/acsbiomaterials.1c01603
ACS Biomater. Sci. Eng. XXXX, XXX, XXX−XXX

switch at the concentration far below the daily therapeutic human dose administered in patients with rheumatism (300−500 10^{-3} g 10^{-3} L 2−5 times/day).

3.1. Electronic Molecular Structure of Fe_3O_4-rGO-SA Nanoparticles. For the formation of Fe_3O_4-rGO-SA NPs, we have prepared GO with a few layer-wrinkled graphene sheets of partially reduced carbon basal planes caused by the removal of functional groups, the C/O = 1.44 atomic ratio, and an average size of ∼202 ± 40 nm (Figure S1, see more details in the Supporting Information). Control experiments were performed without GO, resulting in the formation of Fe_3O_4-SA NPs, and without SA, yielding bare Fe_3O_4 and Fe_3O_4-rGO NPs. Spherical Fe_3O_4-rGO-SA NPs have a smaller average size ⟨d⟩ of ∼10.46 ± 2.77 nm (Figure 1A,B) than Fe_3O_4-SA (∼15.62 ± 4.48 nm) (Figure S2) and are composed of a Fe_3O_4 crystalline phase (amcsd 0007421) with calculated interplanar d spacing values comparable with Fe_3O_4 and Fe_3O_4-SA (Figure 1C and Table S1). The XRD patterns of both types of NPs show a small (221) reflex of SA at $2\theta_B$ = 28.27 and 28.37,[42] indicating complexation of SA to Fe_3O_4. The determined size t of ∼10.20 nm of Fe_3O_4-rGO-SA (Figure S3) is comparable with their average diameter (∼10.46 nm), indicating the uniform 3D space structure of NPs. In contrast, the t value of Fe_3O_4-SA is smaller (∼9.84 nm) than the average diameter (∼15.62 nm), which is presumably caused by a narrower width of these NPs. Fe_3O_4-rGO-SA NPs have a smaller size because of two possible reasons: (i) pH-size dependent amphiphilicity of rGO and (ii) the relationship between the surface activity of rGO and energy of cavitation bubbles. rGO is considered an amphiphilic molecule with a pH-dependent surface activity. Smaller rGOs have increased the edge-to-area ratio and charge density; therefore, they are more hydrophilic at higher pH values. Indeed, the pH values of aqueous Fe_3O_4-rGO-SA and Fe_3O_4-SA NPs were 5 and 4, respectively, indicating that Fe_3O_4-rGO-SA should be more hydrophilic due to their smaller size. On the other hand, rGO can enhance the effects of reduced surface tension on cavitation bubbles with adsorbed SA molecules and can lead to a decreased Laplace pressure. As a result, bubbles with a larger size will be formed. Larger bubbles will release a higher energy at collapse, producing a high local pressure gradient and shock waves, which decrease the NPs' size.

To gain a deeper insight into the molecular complexation of SA with Fe_3O_4 and rGO, we performed FT-IR transmittance spectroscopy analysis of Fe_3O_4-rGO-SA (Figure 1D) in comparison with Fe_3O_4-SA NPs (Figure S4). The FT-IR spectrum of Fe_3O_4-rGO-SA NPs shows the characteristic ν(Fe−O) bonds in bidentate and bridged Fe(III)-bis-salicylato-diaquo complexes and the characteristic ν(Fe−O) stretching band of Fe_3O_4 (574 cm^{-1}) in contrast to Fe_3O_4-SA NPs.[43,44] Another characteristic band of Fe_3O_4 (626 cm^{-1}), which can be assigned to the O═C−O group in-plane bending of SA, is observed as a shoulder in Fe_3O_4-rGO-SA.[45]

In our work, the O−O distances in close packed anion Fe(III) arrays in the octahedral coordination of Fe_3O_4 are 0.294 nm (Fe_3O_4-SA) and 0.296 nm (Fe_3O_4-rGO-SA) (Table S1), which are in good agreement with the O−O distance of magnetite (0.29 nm) reported in the literature.[41] The fundamental vibrations of the $_\nu(O_2)$ "peroxo" complexes[46] of SA and Fe−O in FeO_2 appear as weak bands in both types of NPs due to ultrasonic oxidation in specific binding of SA. However, the C−O stretching coupled with the in-plane deformation of the phenolic OH group (∼1240−1244 cm^{-1}), which is indicative of the intramolecular hydrogen bonding in salicylate, is more pronounced in Fe_3O_4-rGO-SA than in Fe_3O_4-SA. These findings demonstrate the role of rGO in complexation of SA in NPs.

The symmetric $_{\nu s}$(C−O) stretching of the carboxylic group of SA becomes weaker and broader in Fe_3O_4-rGO-SA (∼1317−1377 cm^{-1}) involving the in-plane O−H bending, which was identified in Fe_3O_4-GO NPs by other researchers.[47] The strong band at 1458 cm^{-1} shows the in-plane $_\delta$COO bending of the salicylate monoanion in Fe_3O_4-rGO-SA with complexed SA through the phenolic ring and hydroxyl group. However, the vibrations of Fe(III)-bis-salicylato-diaquo complexes appear stronger in Fe_3O_4-SA NPs in contrast to the phenolic ring vibration $_\nu$(C−H) in Fe_3O_4-rGO-SA. From these results, we conclude that the surface oxygen functional groups of rGO contribute to the specific ultrasonic reduction of Fe(II) in contact with SA ligands and allow the formation of the thermodynamically stable metallocomplex in NPs.

Analysis of the Raman spectra confirms the formation of Fe_3O_4 phase (∼670 cm^{-1})[48] and shows γ-Fe_2O_3 (∼350 cm^{-1})[49] and α-FeOOH (∼492 cm^{-1}) on the surface of Fe_3O_4-rGO-SA NPs caused by natural oxidation of magnetite[50] (Figure 1E and Table S2). In addition, several C−C peaks arising from the vibrations of the benzene ring and solid SA crystal (∼707 cm^{-1}),[51] the C−O stretching of the carboxylic acid group (∼1328 cm^{-1}), and a distinct peak at ∼1600 cm^{-1} appearing from the E_{2g} G mode in rGO due to amorphization of graphite with sp^2-hybridization[52] were detected in Fe_3O_4-rGO-SA NPs. A small peak at 1153 cm^{-1} can be assigned to the nanocrystalline diamond.[53]

The UV−Vis absorbance spectrum of the aqueous colloidal Fe_3O_4-rGO-SA solution shows two characteristic peaks at 231 and 297 nm, which can be assigned to pristine SA,[54] but are slightly shifted in comparison with the observed spectra in phosphate buffer solution at pH 6.8[55] (Figure 1F). The first band can be related to the interaction of the hydroxyl groups with aromatic rings.[56] A broad small peak near 385 nm (∼3.2 eV) indicates the $Fe^{3+}{}_B(e_g\downarrow) \rightarrow Fe^{3+}{}_A(e_g\downarrow, t_2\downarrow)$ interband transitions of Fe_3O_4,[57] and its shift at 390 nm (∼3.18 eV) can be caused by the interaction with rGO in Fe_3O_4-rGO-SA NPs.

Analysis of the EDX spectra showed the following concentration (at.%) of elements in these NPs: O (∼59.2), Fe (∼30.2), and C (∼10.1) with negligible traces of K (∼0.2) and Cl (∼0.4) comparable with Fe_3O_4-SA NPs (Figure S5). Both types of NPs are mainly composed of O, Fe, and C elements but have different O/Fe atomic ratios, ∼1.65 in Fe_3O_4-SA and ∼1.96 in Fe_3O_4-rGO-SA, than bare magnetite NPs (∼1.44),[58] demonstrating the excess of O caused by the complexed SA. The O/C atomic ratio of Fe_3O_4-rGO-SA (∼20.59) is by factor of 3.5 larger than that of Fe_3O_4-SA (∼5.86), proving the complexation of SA with rGO and Fe_3O_4.

3.2. Concentration of Complexed SA Molecules in Fe_3O_4-rGO-SA NPs. The next question to answer is how many SA molecules are complexed in NPs. We assume that for Fe_3O_4-rGO-SA NPs (∼10 nm), the total average density of bulk GO is ∼47.42 × 10^{23} L^{-1}, and the volume of a single NP is ∼5.23 × 10^{-25} m^3 with ∼6.24 × 10^6 iron atoms and ∼8.39 × 10^7 oxygen atoms. The volume of a single GO sheet is ∼4.04 × 10^{-25} m^3, assuming the covalent C−C distance of graphene hexagon of ∼0.142 × 10^{-9} m, the C−H of a benzene ring of ∼0.108 × 10^{-9} m, and diameter of ∼0.426 × 10^{-9} m. One single GO NP consists of 6.49 × 10^7 oxygen atoms and 3.21 × 10^5 carbon atoms if the volume of one single carbon atom is

https://doi.org/10.1021/acsbiomaterials.1c01603
ACS Biomater. Sci. Eng. XXXX, XXX, XXX−XXX

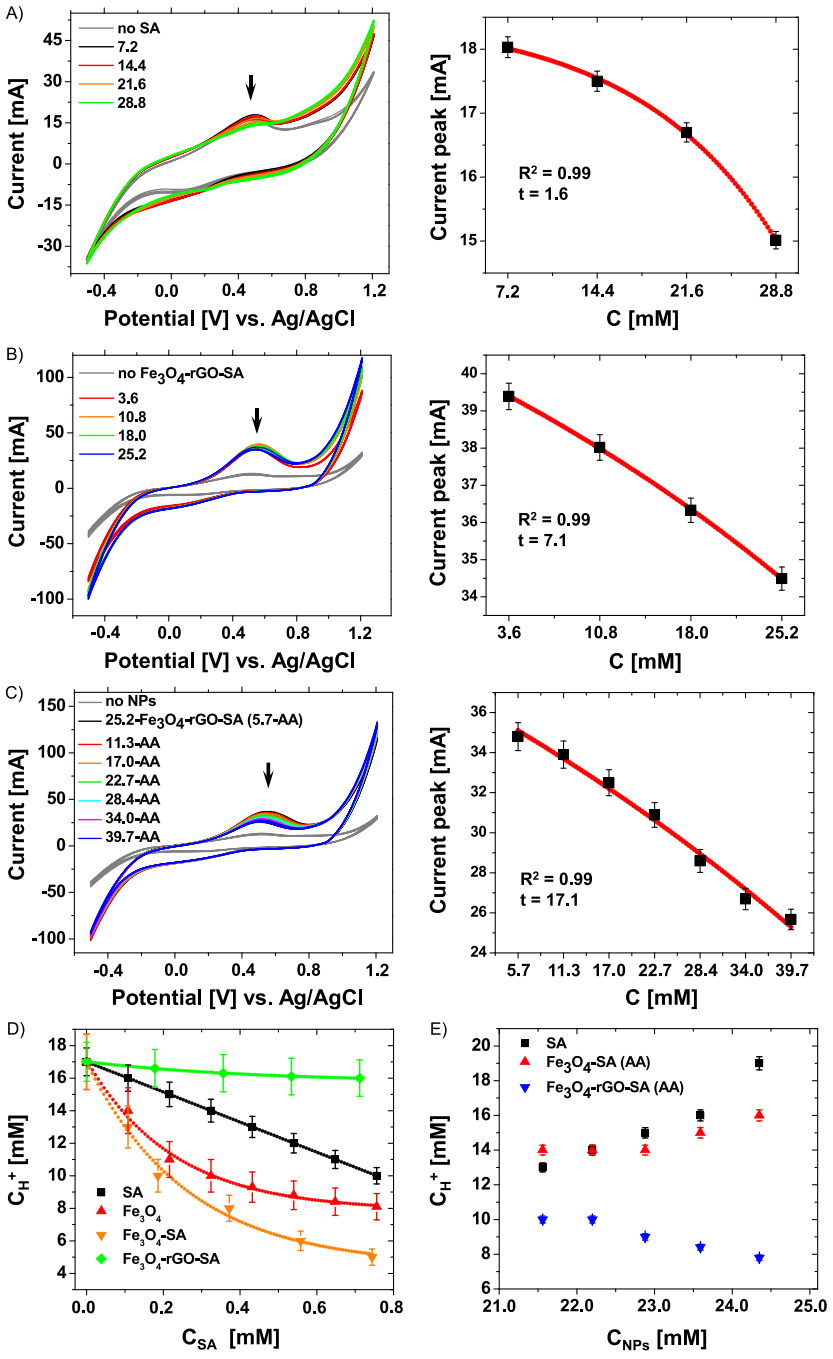

Figure 2. (A) The relative response of current ($\times 10^{-3}$ A) is recorded in aqueous solutions of pristine SA (7.2, 14.4, 21.6, and 28.8 mM) in an applied voltage (from −0.5 to +1.2 V) and the corresponding current peak values ($\times 10^{-3}$ A) of $^{\bullet}$OH formation in these SA aqueous solutions are shown. (B, C) The relative response of current ($\times 10^{-3}$ A) is recorded in aqueous solutions of Fe_3O_4-rGO-SA NPs (3.6−25.2 mM) before and after stepwise addition of ascorbic acid solution (5.7−39.7 mM) and the corresponding current $^{\bullet}$OH peak values ($\times 10^{-3}$ A) versus the concentration of NPs. (D) The plot shows the dependence of the H^+ concentration ($\times 10^{-3}$M) on complexed SA molecules in Fe_3O_4-rGO-SA and Fe_3O_4-SA NPs in comparison with pristine SA and bare Fe_3O_4 NPs in aqueous solution ($\times 10^{-3}$M). The concentration of H^+ ions is theoretically modeled by using the Nernst−Planck equation interface near the electrode surface and electrochemical reactions of oxygen evolution and chlorine production at the anode. (E) The dependence of the theoretically modeled concentration of H^+ ions ($\times 10^{-3}$ M) on nanoparticles ($\times 10^{-3}$ M) in comparison with pristine SA aqueous solution of ascorbic acid is shown.

1.26×10^{-30} m^3. We estimate the density of Fe_3O_4-rGO NPs to be ~5.11×10^{11} L^{-1}, taking into account the complex volume of magnetite and rGO, molecular weights of all components, and the number of iron and oxygen atoms in Fe_3O_4 and carbon and oxygen in rGO. When the density of Fe_3O_4-rGO NPs is divided by the SA density, we have 3.85×10^8 complexed SA molecules. Following a similar procedure of calculation, we estimated the number of complexed SA molecules in Fe_3O_4-SA NPs as ~7.78×10^{10} (Supporting Information). These values of SA molecules in NPs are in good agreement with the concentration of complexed SA molecules estimated from the UV−Vis absorption measurement as 186 μM Fe_3O_4-SA NPs (~25.74 μg/mL) and 178 μM in Fe_3O_4-rGO-SA NPs (~24.56 μg/mL) (Figure S6). However, the

https://doi.org/10.1021/acsbiomaterials.1c01603
ACS Biomater. Sci. Eng. XXXX, XXX, XXX−XXX

measurements of the fluorescence spectra of these NPs in ethanol (70% wt. H_2O) at the same temperature T = 22 °C and pH 5 revealed a higher concentration of complexed SA molecules in Fe_3O_4-rGO-SA (~8.04 μM) and Fe_3O_4-SA (~3.52 μM), showing that Fe_3O_4-rGO-SA NPs have a larger amount of electronically active SA molecules in their complexes than Fe_3O_4-SA (Figure S7).

3.3. Electronic Properties of Fe_3O_4-rGO-SA NPs in the Fenton Process. The catalytic efficiency of Fe_3O_4-rGO-SA NPs to diminish the $^{\bullet}OH$ radical formation was examined in the electro-Fenton process (Figure 2 and Figure S8). The formation of $^{\bullet}OH$ radicals is associated with the characteristic current peak at ~18.51 mA (~0.48 V) due to oxidation and a small broad peak at ~−9.86 mA (~0.18 V) by reduction (Figure 2A). At an increased SA concentration (from 7.2 to 28.8 mM), the oxidation peak disappeared at a reaction rate of ~1.6 and two reduction peaks were developed at ~−9.52 mA (~0.21 V) and ~−4.29 mA (~0.64 V), which indicated the site-specific drug location,[59] caused by the iron binding ability and formation of the SA−Fe(III) complex.[60] The salicylate−iron complex has superoxide-dismutase (SOD) activity, which involves the reduction of the Fe(III) complex to Fe(II), generating $^{\bullet}OH$.[7] SA decreases the flux of hydroxyl radicals through chelation, which causes a redox deactivation mechanism of iron Fenton reaction centers in the reaction $Fe(II) + H_2O_2 \rightarrow Fe(III) + {}^{\bullet}OH + OH^-$.[5] SA enables bringing about the catalytic dismutation of the superoxide radical ($O_2^{\bullet-}$), resulting in its removal depending on iron and the salicylate:iron molar ratio (in our work from 7.2 to 28.8). In contrast to free SA molecules, the iron−salicylate complex does not have the thermodynamic driving force to act as an effective Fenton reagent necessary for the production of damaging oxygen-containing radicals. It was proven that salicylate (in contrast to SA) acts by redox deactivation of iron, not by hydroxyl radical scavenging.

The decrease in the current $^{\bullet}OH$ peak is recorded in CV of Fe_3O_4-rGO-SA NPs (from 3.6 to 25.2 mM) at a higher reaction rate of ~7.1 than pristine SA (Figure 2B). This reaction rate is increased by tenfold (~17.1) when an aqueous solution of Fe_3O_4-rGO-SA NPs (25.2 mM) was stepwise added with AA (5.7−39.7 mM) (Figure 2C). For comparison, Fe_3O_4-SA NPs (25.2 mM) in AA aqueous solution decrease the $^{\bullet}OH$ peak at a reaction rate of ~6.7 (Figure S8). The enhanced catalytic activity of Fe_3O_4-rGO-SA NPs can be caused by the higher concentration of electronically active complexed SA ligands (~8.04 μM) than in Fe_3O_4-SA (~3.52 μM) that can reduce iron and activate AA against OH generation. In addition, the formation of Fe(III)-bis-salicylato-diaquo complexes is more pronounced in Fe_3O_4-SA than in Fe_3O_4-rGO-SA NPs, meaning that ferric complexes are not reduced by $O_2^{\bullet-}$ ions acting as a precursor to H_2O_2 in superoxide dismutation, thereby promoting the Fenton reaction.

Those NPs that have ferrous-SA complexes and adsorbed AA molecules contribute to the $^{\bullet}OH$ radical damage, in contrast to Fe_3O_4 and Fe_3O_4-SA NPs (7.2−28.8 mM), which promote the $^{\bullet}OH$ growth at the reaction rates of ~6.3 and ~3.2. As a result, rGO may strongly diminish $^{\bullet}OH$ radicals in contact with AA and ascorbate free radicals ($AscH^{\bullet-}$), which reduce the Fe(III) complex to Fe(II), maintaining the generation of soluble Fe(II) in the iron oxide system.[18] In addition, AA can directly react with $^{\bullet}OH$, superoxide, and $^1O_2$ via the ascorbate−glutathione pathway, mitigating oxidative stress.[19]

To understand the antioxidant activity of Fe_3O_4-rGO-SA NPs, the oxygen evolution reaction at the anode resulting in H^+ formation is theoretically modeled (Figure 2D). The computed H^+ profile depends on the molecular state of SA and its concentration during the electrochemical reaction. The amounts of H^+ ions (C_{H+}, $\times 10^{-3}$ M) versus SA (C_{SA}, $\times 10^{-3}$ M) complexed in Fe_3O_4-SA and Fe_3O_4-rGO-SA NPs are calculated in comparison with Fe_3O_4 and pristine drug. Analysis of modeling shows the decreased C_{H+} values at elevated C_{SA} of pristine or complexed SA in NPs at different reaction rates. The C_{H+} decrease by pristine SA (black) is accurately fitted to a linear function at a higher reaction rate of ~9.26 than Fe_3O_4 and Fe_3O_4-SA NPs by performing the fit to the exponential decay function at the reaction rates of ~0.23 and ~0.26. The lowest amount of H^+ ions (~5.1×10^{-3} M) is produced by Fe_3O_4-SA NPs with ~0.7×10^{-3} M by complexed SA in contrast to ~10.8×10^{-3} M by pristine SA. However, Fe_3O_4-rGO-SA NPs produce ~16.0×10^{-3} M of H^+ ions at a reaction rate of ~0.45 due to a twofold faster charge transfer in dismutation reaction of the SA−iron complex and interfere with H_2O_2 signaling.[5,7] Stable production of higher amounts of H^+ at the ultrasonically formed iron−SA complex in Fe_3O_4-rGO-SA than Fe_3O_4-SA NPs or pristine SA molecules can cause redox deactivation of iron in the Fenton process because of the electronic-molecular structure of NPs.

Two opposite mechanisms of H^+ ion production by Fe_3O_4-SA (red) or Fe_3O_4-rGO-SA (blue) NPs (21.55−24.36 $\times 10^{-3}$ M) are observed in AA aqueous solutions (Figure 2E). The molar C_{H+} is increased by pristine SA (~13.0−19.0 $\times 10^{-3}$M) or Fe_3O_4-SA NPs (14.0−16.0 $\times 10^{-3}$ M), but it is decreased by Fe_3O_4-rGO-SA NPs (9.9−7.8 $\times 10^{-3}$ M), demonstrating that AA may act as an electronic molecular switch of the antioxidant activity of two different mechanisms in a concentration-dependent manner. The adsorbed AA molecules on the surface of Fe_3O_4-rGO-SA interact with the iron−SA complexes of NPs and cause the decreased generation of H^+ and diminishing of hydroxyl radicals in Fenton, thereby enhancing the protective antioxidant mechanism of ascorbate: ascorbate $+2H^+ + O_2^{\bullet-} \rightarrow 2\ H_2O_2$ + dehydroascorbate, excluding oxidation of ascorbate at pH 5.[20]

To understand the electrokinetic activity of NPs in diminishing of hydroxyl radicals, the ξ-potential values of Fe_3O_4-SA and Fe_3O_4-rGO-SA were determined in comparison with bare Fe_3O_4 and Fe_3O_4-rGO NPs. The ξ-potential values of bare NPs change in the following order: −38.8 ± 3.0 mV (Fe_3O_4) and −29.7 ± 2.3 mV (Fe_3O_4-rGO) (Figure S9). The ξ-potential values of iron−SA complexes become more positive depending on the type of ultrasonic complexation and NP's structure and concentration (−10.2 ± 0.8 mV (Fe_3O_4-SA, when SA was added during ultrasonic treatment of the preformed Fe_3O_4 phase) and 12.2 ± 0.9 mV (Fe_3O_4-SA, with complexed SA molecules during the synthesis of NPs)) and can linearly increase up to 29.4 ± 1.5 mV at a concentration of 15.9 μg/mL (Table S3 and Figure S10A). In contrast, the ξ-potential values of iron−SA complexes in the in situ formed Fe_3O_4-rGO-SA structure change from −5.7 ± 2.6 to 12.1 ± 1.0 mV as the concentration of NPs nonlinearly increased from 6.3 to 250 μg/mL (Table S4 and Figure S10B). Therefore, a more acidic environment is formed in colloidal Fe_3O_4-rGO-SA than in Fe_3O_4-SA solution, which can change the adsorption of AA molecules on NPs and switch between the redox deactivation

https://doi.org/10.1021/acsbiomaterials.1c01603
ACS Biomater. Sci. Eng. XXXX, XXX, XXX−XXX

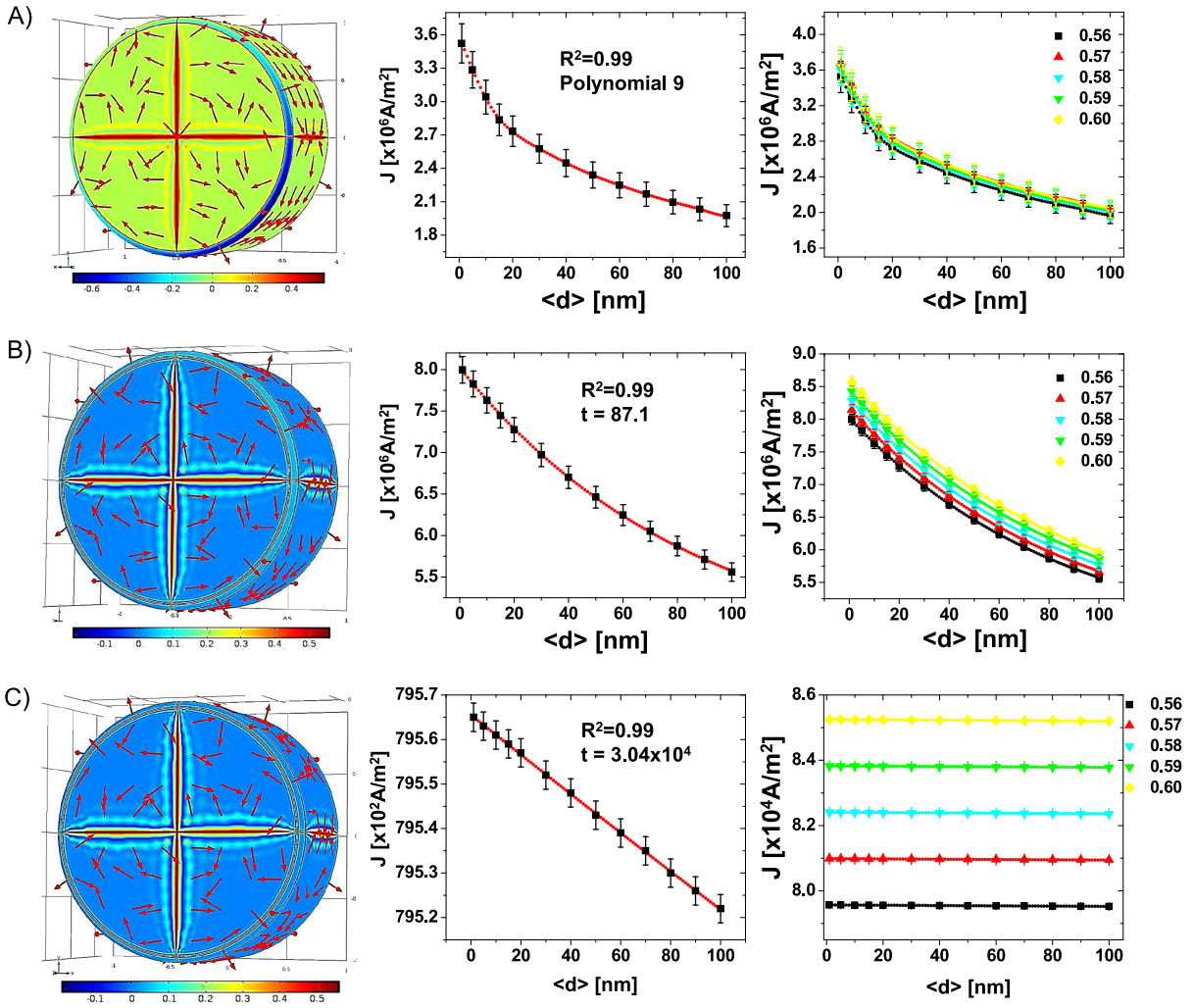

Figure 3. The 3D plots of the computed electric surface potential distribution (U) on (A) bare Fe_3O_4 (~30 nm), Fe_3O_4-SA (~15 nm), and Fe_3O_4-rGO-SA (~10 nm) NP cross sections along the *yz* plane at an initial potential value of 0.56 V corresponding to the •OH formation are shown. The dependence of *J* ($\times 10^6$ A m^{-2}) magnitudes versus the average diameters of NPs (⟨d⟩, 1−100 nm) is theoretically modeled in the potential range (0.56−0.60 V).

of iron (more acidic) or antioxidation (more basic) mechanisms.

3.4. Modeling of the Electric Surface Potential Cross Section of Fe_3O_4-rGO-SA NPs. Therefore, the next question to answer is why does the electronic AA donor accelerate the diminishing reaction of •OH radicals in contact with complexed SA in the iron oxide system of rGO. To assess the charge carrier density with such surfaces, we performed the computation based on the 3D modeling of the electric surface potential cross section distribution (U) on Fe_3O_4-rGO-SA in comparison with Fe_3O_4 and Fe_3O_4-SA NPs (Figure 3). Analysis of the 3D U distribution modeling shows that peak magnitudes appear only in the cross section regions of NPs. The derived current *J* density peak magnitudes are the highest if ⟨*d*⟩ of NPs approaches 1 nm: 3.52×10^6 A m^{-2} (Fe_3O_4), 7.45×10^6 A m^{-2} (Fe_3O_4-SA), and 7.97×10^4 A m^{-2} being two orders of magnitude lower in Fe_3O_4-rGO-SA, which is determined by the rGO physical properties.

The computed *J* values nonlinearly decrease with increased ⟨*d*⟩ of NPs up to 100 nm at reaction rates: by fitting to a polynomial function of the 9th order on Fe_3O_4, ~87 and ~3×10^4 by fitting to the exponential decay function on Fe_3O_4-SA and Fe_3O_4-rGO-SA (more details in the Supporting Information, p.S21). The *J* magnitudes decrease on Fe_3O_4-rGO-SA in a small range (from 795.65×10^2 to 795.22×10^2 A m^{-2}) in contrast to Fe_3O_4-SA (from 7.99×10^6 to 5.55×10^6 A m^{-2}), demonstrating the important role of rGO and complexed SA in enhanced charge transfer catalysis.

3.5. Intracellular Accumulation and Cytotoxicity of Fe_3O_4-rGO-SA NPs. As we have shown that we can control the •OH and H^+ production by Fe_3O_4-rGO-SA NPs, it appears promising to advance this method for the growth inhibition study of HeLa, HepG2, and HT29 cancer cells with internalized NPs (Figure 4; Figures S11, S12, and S13). Most of the cells exhibit bright fluorescence signals over their entire surface structure, proving the successful intracellular accumulation of NPs (Table S5). Very few non-fluorescent parts inside the cells can be detected arising from the intracellular vesicular structures. There are clear changes of the morphology of cells caused by their interaction with digested NPs with respect to control live cells (without NPs). These morphological changes are distinctly seen in HepG2 cells (Figure 4D,E) in comparison with the morphology of non-fluorescent NPs. Therefore, one may conclude that this effect can be caused by the toxicity of the dye itself. Overall, the dye color distribution in the images is relatively uniform in

https://doi.org/10.1021/acsbiomaterials.1c01603
ACS Biomater. Sci. Eng. XXXX, XXX, XXX−XXX

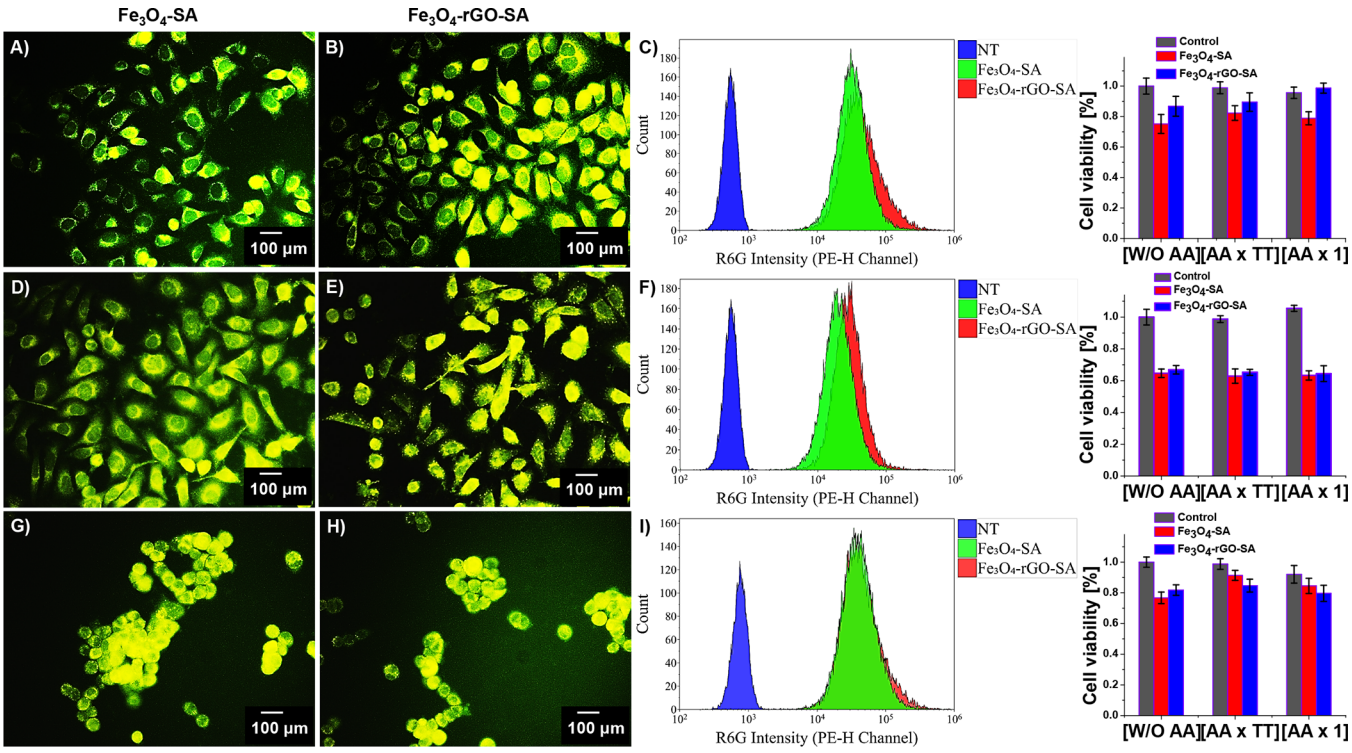

Figure 4. Representative fluorescence microscopy images of (A, B) HeLa, (D, E) HepG2, and (G, H) HT29 cancer cells with internalized Fe_3O_4-SA or Fe_3O_4-rGO-SA NPs (~35 μg mL^{-1}) after modification with rhodamine 6G (R6G) dye are shown. (C, F, I) Statistical histograms of fluorescence signals obtained from flow cytometry measurements of these cells with untreated (NT) or internalized Fe_3O_4-SA or Fe_3O_4-rGO-SA NPs are shown with diagrams of cell viability with the control cells without NPs (gray) at conditions without ascorbic acid (W/O AA), in ascorbic acid aqueous solution (15 μg/mL) via titration (AA × TT), and at once method (AA × 1).

all three lines, despite the fact that HT29 cells (Figure 4G,H) grow in dense clusters with the surrounded mucous-like membrane. In our experiments, the initial number of HT29 cells was insufficient to form multiple dense clusters during the incubation period.

After 24 h of incubation in HeLa cells, the fluorescence images revealed a clear difference between the internalized Fe_3O_4-SA and Fe_3O_4-rGO-SA NPs (Figure 4A,B). In particular, ~47% of HeLa cells with intracellularly accumulated Fe_3O_4-rGO-SA NPs and only ~22% with Fe_3O_4-SA NPs exhibited the brightest fluorescence over the entire surface, demonstrating that these NPs degraded inside the cells and left only dye molecules. In contrast to HeLa cells, almost all of HepG2 cells with intracellularly accumulated Fe_3O_4-rGO-SA NPs showed the brightest fluorescence as individual bright dots in the cytosol and nucleus and as a solid bright spot over the entire surface (Figure 4D,E). For comparison, no individual bright dots were observed in bright fluorescent HepG2 cells with Fe_3O_4-SA NPs. The mean numbers of fluorescent cells with brightness over the entire surface were ~38% with Fe_3O_4-rGO-SA and ~23% with Fe_3O_4-SA NPs. The presence of individual fluorescent dots that are homogeneously distributed in the cytosol and nucleus of HepG2 cells indicated that Fe_3O_4-rGO-SA NPs are not fully digested in the intracellular compartments after 24 h of incubation in most of these cells. This is in contrast to Fe_3O_4-SA NPs, which are fully digested by HepG2 cells, leaving dye molecules inside the cells. No significant differences in intracellularly digested Fe_3O_4-rGO-SA or Fe_3O_4-SA NPs were observed in HT29 cells (Figure 4G,H). NPs with loaded SA molecules were more strongly accumulated inside the cells than bare NPs according to the data shown in Table S5. At the same time, NPs with rGO showed an advantage in comparison with iron oxide NPs.

Analysis shows that Fe_3O_4-rGO-SA NPs are stronger internalized, which can be explained by the enhanced interaction of rGO with the biological membrane and its interference with the cell signaling processes observed in intracellular studies of various graphene oxide−magnetite−drug NPs.[31] The longer retention period of drug within the cells was ascribed to the effects of graphene-based nanocarriers, resulting in a higher intracellular concentration of this drug. Another evidence of the greater interaction of graphene-based NPs with biological membranes was derived from the confocal microscopy studies: graphene-based nanocarriers comparatively required a longer time to gain access in the HeLa cells, which is a strong indication of its improved interaction with the membrane lipid layer. In the study of nuclear apoptosis of HepG2 cells with stronger internalized Fe_3O_4-rGO-based drug NPs, condensed and disintegrated nuclei and chromatin were observed from the apoptotic nuclei at the membrane boundaries.[61] The study on the interaction of GO with mammalian HT-29 cells reveals that GO promotes cell attachment and proliferation.[62] The complex based on the drug−GO−Fe_3O_4 structure advantageously reduced the viability of HT29 cells in comparison with bare drug−GO NPs and free drug.[63]

In the HeLa line, Fe_3O_4-rGO-SA NPs reproducibly decrease the number of cells by ~14% without the adsorbed AA molecules, which is in contrast to Fe_3O_4-rGO-SA-AA in the titration procedure, suggesting that the redox deactivation of

https://doi.org/10.1021/acsbiomaterials.1c01603
ACS Biomater. Sci. Eng. XXXX, XXX, XXX−XXX

iron and not enhanced antioxidation can be a dominant mechanism of in vitro growth inhibition (Figure 4C).

In contrast to HeLa and HT29 cells, stronger cytotoxicity effects of ∼67% were determined in HepG2 with Fe_3O_4-rGO-SA NPs in an AA-independent manner, suggesting that the mechanism of redox deactivation of iron at increased H^+ contributes more to the growth inhibition of cancer cells through the decreased formation of hydroxyl radicals (Figure 4F).

In all cells, the control experiments of pristine AA titration or SA did not reveal any statistically relevant changes. A slight decrease of cell viability (∼0.92 ± 0.06%) was detected when AA was added at once, indicating the intracellular induction of reduction processes. In the absence of AA, the overall cytotoxic effects were stronger with intracellularly internalized Fe_3O_4 than Fe_3O_4-rGO (Figures S12 and S13), which can be caused by the higher amount of hydroxyl radical production.

In HT29 cells, the cytotoxicity of Fe_3O_4-SA without AA addition (∼65%) was comparable to that of Fe_3O_4-rGO-SA NPs (∼63%), demonstrating the important role of site-specific Fe^{2+}− and Fe^{3}−salicylate complexes in the generation of damaging oxygen-containing radicals (e.g., malignant neoplasm H_2O_2 and super oxide O_2^- ions) that are released as byproducts of normal respiratory cellular function, causing oxidative tissue damage (Figure 4F). However, the cytotoxicity of Fe_3O_4-rGO-SA was enhanced in comparison with Fe_3O_4-SA NPs when AA was added during titration, and this effect was more pronounced at one addition. The addition of AA in HT29 cancer cells caused switchable growth inhibition by Fe_3O_4-rGO-SA (∼85%, ∼80%) with respect to Fe_3O_4-SA (∼91%, ∼85%), demonstrating that enhanced antioxidation with the decreased H^+ generation can be the prevailing mechanism of antiproliferative activity of NP in vitro.

4. CONCLUSIONS

We have developed a single-step ultrasonic method (20 kHz) for in situ complexation of pristine SA molecules during the growth of Fe_3O_4-rGO NPs (∼10 nm). SA ligands are selectively complexed with Fe(III)/Fe(II) binding sites as the integral parts of NPs with a precisely defined electronic molecular structure. Fe_3O_4-rGO-SA NPs act as the redox deactivators of iron centers and increase the H^+ generation, resulting in efficient diminishing of $^{\bullet}OH$ radicals. This property of Fe_3O_4-rGO-SA NPs is tenfold stronger in comparison with pristine SA molecules when ascorbic acid molecules adsorbed on the NP's surface in an aqueous solution that causes enhanced antioxidation and decreased the formation of H^+ ions. Ascorbic acid molecules act as the antioxidant molecular switches of H^+ production by Fe_3O_4-rGO-SA NPs due to the four orders of magnitude larger electric surface potential on their surface, where rGO plays an important role in enhanced charge transfer catalysis. Most significantly, Fe_3O_4-rGO-SA NPs are nontoxic to erythrocytes, i.e., human peripheral blood mononuclear cells, and can surpassingly inhibit the growth of three cancer cell lines: HeLa, HepG2, and HT29 than pristine SA. This approach can be successfully expanded to many other NSAIDs to better understand the intracellular drug−enzyme, drug−metal, and drug−cancer intracellular interactions, which can be particularly useful in the treatment of diabetes, rheumatism, and liver and oncological diseases.

■ ASSOCIATED CONTENT

Supporting Information

The Supporting Information is available free of charge at https://pubs.acs.org/doi/10.1021/acsbiomaterials.1c01603.

Raman and energy dispersive X-ray fluorescence (EDX) spectra of rGO; SEM analysis of Fe_3O_4-SA NPs; XRD analysis of Fe_3O_4-rGO-SA and Fe_3O_4-SA NPs; FTIR FT-IR transmittance spectra of Fe_3O_4-rGO-SA NPs (2400−3800 cm^{-1}) and Fe_3O_4-SA NPs (400−3800 cm^{-1}); Raman and EDX spectra of NPs; UV−Vis absorption spectra of aqueous solutions of NPs; cyclic voltammograms of the electro-Fenton process with bare Fe_3O_4-SA NPs before and after stepwise addition of ascorbic acid aqueous solution; and optical phase contrast and fluorescence images and statistical diagrams of live HeLa, HepG2, and HT29 cancer cells with incubated NPs (PDF)

■ AUTHOR INFORMATION

Corresponding Author

Darya Radziuk − *Laboratory of Integrated Micro- and Nanosystems, Belarusian State University of Informatics and Radioelectronics, 220013 Minsk, Republic of Belarus;* orcid.org/0000-0001-7287-4303; Email: radziuk@bsuir.by

Authors

Lubov Mikhnavets − *Laboratory of Integrated Micro- and Nanosystems, Belarusian State University of Informatics and Radioelectronics, 220013 Minsk, Republic of Belarus*

Viktar Abashkin − *Institute of Biophysics and Cell Engineering of National Academy of Sciences of Belarus, 220072 Minsk, Republic of Belarus*

Hanna Khamitsevich − *Department of Microbiology, Belarusian State University, 220030 Minsk, Republic of Belarus*

Dzmitry Shcharbin − *Institute of Biophysics and Cell Engineering of National Academy of Sciences of Belarus, 220072 Minsk, Republic of Belarus*

Aliaksandr Burko − *Laboratory of Applied Plasmonics, Belarusian State University of Informatics and Radioelectronics, 220013 Minsk, Republic of Belarus*

Nina Krekoten − *Scientific-Technical Center "Belmicrosystems", 220108 Minsk, Republic of Belarus*

Complete contact information is available at: https://pubs.acs.org/10.1021/acsbiomaterials.1c01603

Author Contributions

The manuscript was written through the contributions of all authors.

Notes

The authors declare no competing financial interest.

■ ACKNOWLEDGMENTS

This work is supported by the Belarusian Fundamental Research Programs via grant nos. 21-3051 57 031.00, 21-3163M, B20SLKG-002, B21KORG-001, B21TUB-001, B21RM-045, and B21M-001 and the Polish National Agency for Academic Exchange EUROPARTNER grant no. PPI/APM/2018/1/00007/U/001. We acknowledge Prof. L. Ivashkevich for the XRD measurements and Prof. M. Artemyev for the insightful comments (Belarusian State University), Prof.

V. Bondarenko for access to the Metrohm Autolab potentiostat/galvanostat instrument, and Dr. L. Tabulina and Anastasia Tkach for the synthesis of bulk GO (Belarusian State University of Informatics and Radioelectronics).

REFERENCES

(1) Rena, G.; Sakamoto, K. Salicylic acid: old and new implications for the treatment of type 2 diabetes? *Diabetol. Int.* **2014**, *5*, 212−218.
(2) Bashir, A. I. J.; Kankipati, C. S.; Jones, S.; Newman, R. M.; Safrany, S. T.; Perry, C. J.; Nicholl, I. D. A novel mechanism for the anticancer activity of aspirin and salicylates. *Int. J. Oncol.* **2019**, *54*, 1256−1270.
(3) Nyúl, E.; Kuzma, M.; Mayer, M.; Lakatos, S.; Almási, A.; Perjési, P. HPLC study on Fenton-reaction initiated oxidation of salicylic acid. Biological relevance of the reaction in intestinal biotransformation of salicylic acid. *Free Radical Res.* **2018**, *52*, 1−261.
(4) Van Jaarsveld, H.; Kuyl, J. M.; van Zyl, G. F.; Barnard, H. C. Salicylate in the perfusate during ischemia/reperfusion prevented mitochondrial injury. *Res. Commun. Mol. Pathol. Pharmacol.* **1994**, *86*, 287−295.
(5) Cheng, I. F.; Zhao, C. P.; Amolins, A.; Galazka, M.; Doneski, L. A hypothesis for the *in vivo* antioxidant action of salicyclic acid. *BioMetals* **1996**, *9*, 285−290.
(6) Shi, X.; Ding, M.; Dong, Z.; Chen, F.; Ye, J.; Wang, S.; Leonard, S. S.; Castranova, V.; Vallyathan, V. Antioxidant properties of aspirin: characterization of the ability of aspirin to inhibit silica-induced lipid peroxidation, DNA damage, NF-kappaB activation, and TNF-alpha production. *Mol. Cell. Biochem.* **1999**, *199*, 93−102.
(7) Jay, D.; Jay, E. G.; Medina, M. A. Superoxide dismutase activity of the salicylate-iron complex. *Arch. Med. Res.* **1999**, *30*, 93−96.
(8) Sullivan, M. P.; Holtkamp, H. U.; Hartinger, C. G. Antitumor metallodrugs that target proteins. *Met. Ions Life Sci.* **2018**, *18*, 351−386.
(9) Boros, E.; Dyson, P. J.; Gasser, G. Classification of metal-based drugs according to their mechanisms of action. *Chem* **2020**, *6*, 41−60.
(10) Janoš, P.; Spinello, A.; Magistrato, A. All-atom simulations to studying metallodrugs/target interactions. *Curr. Opin. Chem. Biol.* **2021**, *61*, 1−8.
(11) Stathopoulou, M.-E. K.; Banti, C. N.; Kourkoumelis, N.; Hatzidimitriou, A. G.; Kalampounias, A. G.; Hadjikakou, S. K. Silver complex of salicylic acid and its hydrogel-cream in wound healing chemotherapy. *J. Inorg. Biochem.* **2018**, *181*, 41−55.
(12) Banti, C. N.; Papatriantafyllopoulou, C.; Tasiopoulos, A. J.; Hadjikakou, S. K. New metalo-therapeutics of NSAIDs against human breast cancer cells. *Eur. J. Med. Chem.* **2018**, *143*, 1687−1701.
(13) Wu, X.-W.; Zheng, Y.; Wang, F.-X.; Cao, J.-J.; Zhang, H.; Zhang, D.-Y.; Tan, C.-P.; Ji, L.-N.; Mao, Z.-W. Anticancer IrIII−aspirin conjugates for enhanced metabolic immuno-modulation and mitochondrial lifetime imaging. *Chem. − Eur. J.* **2019**, *25*, 7012−7022.
(14) Deng, J.; Gou, Y.; Chen, W.; Fu, X.; Deng, H. The Cu/ligand stoichiometry effect on the coordination behavior of aroyl hydrazone with copper(II): Structure, anticancer activity and anticancer mechanism. *Bioorg. Med. Chem.* **2016**, *24*, 2190−2198.
(15) Pereira, T. A.; Teixeira da Silva, G. E.; Hernández, R. B.; Forti, F. L.; Espósito, B. P. Antitumor activity of Mn (III) complexes in combination with phototherapy and antioxidant therapy. *BioMetals* **2013**, *26*, 439−446.
(16) McCarty, M. F.; Contreras, F. Increasing superoxide production and the labile iron pool in tumor cells may sensitize them to extracellular ascorbate. *Front. Oncol.* **2014**, *4*, 249.
(17) Chen, Q.; Espey, M. G.; Krishna, M. C.; Mitchell, J. B.; Corpe, C. P.; Buettner, G. R.; Shacter, E.; Levine, M. Pharmacologic ascorbic acid concentrations selectively kill cancer cells: action as a pro-drug to deliver hydrogen peroxide to tissues. *PNAS* **2005**, *102*, 13604−13609.
(18) Hou, X.; Huang, X.; Ai, Z.; Zhao, J.; Zhang, L. Ascorbic acid/Fe@Fe_2O_3: A highly efficient combined Fenton reagent to remove organic contaminants. *J. Hazard. Mater.* **2016**, *310*, 170−178.
(19) Dewhirst, R. A.; Fry, S. C. The oxidation of dehydroascorbic acid and 2,3-diketogulonate by distinct reactive oxygen species. *Biochem. J.* **2018**, *475*, 3451−3470.
(20) Halliwell, B.; Foyer, C. H. Ascorbic acid, metal ions and the superoxide radical. *Biochem. J.* **1976**, *155*, 697−700.
(21) Wu, T.-M.; Liu, S.-T.; Chen, S.-Y.; Chen, G.-S.; Wu, C.-C.; Huang, S.-M. Mechanisms and applications of the anti-cancer effect of pharmacological ascorbic acid in cervical cancer cells. *Front. Oncol.* **2020**, *10*, 1483.
(22) Belin, S.; Kaya, F.; Duisit, G.; Giacometti, S.; Ciccolini, J.; Fontés, M. Antiproliferative effect of ascorbic acid is associated with the inhibition of genes necessary to cell cycle progression. *PLoS ONE* **2009**, *4*, No. e4409.
(23) Hannesschlaeger, C.; Pohl, P. Membrane permeabilities of ascorbic acid and ascorbate. *Biomolecules* **2018**, *8*, 1−11.
(24) Kutuk, O.; Basaga, H. Aspirin inhibits TNFα-and IL-1-induced NF-κB activation and sensitizes HeLa cells to apoptosis. *Cytokine* **2004**, *25*, 229−237.
(25) Giardina, C.; Inan, M. S. Nonsteroidal anti-inflammatory drugs, short-chain fatty acids, and reactive oxygen metabolism in human colorectal cancer cells. *Biochim. Biophys. Acta* **1998**, *1401*, 277−288.
(26) Giardina, C.; Boulares, H.; Inan, M. S. NSAIDs and butyrate sensitize a human colorectal cancer cell line to TNF-α and Fas ligation: the role of reactive oxygen species. *Biochim. Biophys. Acta* **1999**, *1448*, 425−438.
(27) Lewandowski, W.; Kalinowska, M.; Lewandowska, H. The influence of metals on the electronic system of biologically important ligands. Spectroscopic study of benzoates, salicylates, nicotinates and isoorotates. *J. Inorg. Biochem.* **2005**, *99*, 1407−1423.
(28) Englinger, B.; Pirker, C.; Heffeter, P.; Terenzi, A.; Kowol, C. R.; Keppler, B. K.; Berger, W. Metal drugs and the anticancer immune response. *Chem. Rev.* **2019**, *119*, 1519−1624.
(29) Arami, H.; Khandhar, A.; Liggitt, D.; Krishnan, K. M. In vivo delivery, pharmacokinetics, biodistribution and toxicity of iron oxide nanoparticles. *Chem. Soc. Rev.* **2015**, *44*, 8576−8607.
(30) Zanganeh, S.; Hutter, G.; Spitler, R.; Lenkov, O.; Mahmoudi, M.; Shaw, A.; Pajarinen, J. S.; Nejadnik, H.; Goodman, S.; Moseley, M.; Coussens, L. M.; Daldrup-Link, H. E. Iron oxide nanoparticles inhibit tumour growth by inducing pro-inflammatory macrophage polarization in tumour tissues. *Nat. Nanotechnol.* **2016**, *11*, 986−994.
(31) Nandi, S.; Kale, N. R.; Takale, V.; Chate, G. C.; Bhave, M.; Banerjee, S. S.; Khandare, J. J. Cell deformation and acquired drug resistance: elucidating the major influence of drug-nanocarrier delivery systems. *J. Mater. Chem. B* **2020**, *8*, 1852−1862.
(32) Li, D.; Deng, M.; Yu, Z.; Liu, W.; Zhou, G.; Li, W.; Wang, X.; Yang, D.; Zhang, W. Biocompatible and stable GO-coated Fe_3O_4 nanocomposite: a robust drug delivery carrier for simultaneous tumor MR imaging and targeted therapy. *ACS Biomater. Sci. Eng.* **2018**, *4*, 2143−2154.
(33) Fiadosenka, U.; Matsukovich, A.; Tabulina, L.; Labunov, V.; Radziuk, D. The properties of the sonochemically functionalized nonsteroidal anti-inflammatory drug ketorolac in an Fe_3O_4-graphene oxide nanocomposite. *New J. Chem.* **2019**, *43*, 16118−16122.
(34) Tkach, A.; Fiadosenka, U.; Burko, A.; Bandarenka, H. V.; Matsukovich, A.; Krekoten, N.; Tabulina, L.; Labunov, V.; Radziuk, D. Poly(vinyl alcohol) enhances acetylation of ascorbic acid in superparamagnetic graphene oxide nanoparticles ultrasonically complexed with acetylsalicylic acid. *ACS Appl. Polym. Mater.* **2020**, *2*, 3663−3673.
(35) Zeiger, B. W.; Suslick, K. S. Sonofragmentation of molecular crystals. *J. Am. Chem. Soc.* **2011**, *133*, 14530−14533.
(36) Kim, H. N.; Suslick, K. S. Sonofragmentation of ionic crystals. *Chem. − Eur. J.* **2017**, *23*, 2778−2782.
(37) Suslick, K. S.; Schubert, P. F.; Goodale, J. W. Sonochemistry and sonocatalysis of iron carbonyls. *J. Am. Chem. Soc.* **1981**, *103*, 7342−7344.
(38) Suslick, K. S.; Fang, M.; Hyeon, T. Sonochemical synthesis of iron colloids. *J. Am. Chem. Soc.* **1996**, *118*, 11960−11961.

https://doi.org/10.1021/acsbiomaterials.1c01603
ACS Biomater. Sci. Eng. XXXX, XXX, XXX−XXX

(39) Bang, J. H.; Suslick, K. S. Sonochemical synthesis of nanosized hollow hematite. *J. Am. Chem. Soc.* **2007**, *129*, 2242−2243.
(40) Xu, H. X.; Suslick, K. S. Sonochemical preparation of functionalized graphenes. *J. Am. Chem. Soc.* **2011**, *133*, 9148−9151.
(41) Mackay, A. L. Some aspects of the topochemistry of iron oxides and hydroxides. In *Reactivity of solids. Proc. 4th Int*; de Boer, J. H. ed.; Symp. Reactivity of Solids: Amsterdam, 1961, 571−583.
(42) Fukuoka, E.; Makita, M.; Yamamura, S. Evaluation of crystallite orientation in tablets by X-ray diffraction methods. *Chem. Pharm. Bull.* **1987**, *35*, 1564−1570.
(43) Nakamoto, K. *Infrared and Raman spectra of inorganic and coordination compounds*; 4th Ed. John Wiley & Sons, 1984, pp. 264.
(44) Khadikar, P. V.; Ali, S. M.; Heda, B. D. Kinetics of thermal dehydration of some bis-salicylato-diaquo complexes of transition metal ions. *J. Therm. Anal.* **1985**, *30*, 167−176.
(45) Cornell, R. M.; Schwertmann, U. *The Iron oxides: Structure, properties, reactions, occurences and uses*; 2nd edition, Wiley-VCH Verlag GmbH & Co. KGaA: Weinheim, Germany, 2003, pp. 1−199.
(46) Dutta, S. K.; Ghosh, M.; Biswas, P.; Flörke, U.; Saal, C.; Haase, W.; Nag, K. Formation of oxo-bridged tetrairon(III) complexes mediated by oxygen activation. Structure, spectroscopy, magnetism and electrochemistry. *New J. Chem.* **2007**, *31*, 93−101.
(47) Wang, Z.; Zhou, C.; Xia, J.; Via, B.; Xia, Y.; Zhang, F.; Li, Y.; Xia, L. Fabrication and characterization of a triple functionalization of graphene oxide with Fe_3O_4, folic acid and doxorubicin as dual-targeted drug nanocarrier. *Colloids Surf., B* **2013**, *106*, 60−65.
(48) Lia, Y.-S.; Church, J. S.; Woodhead, A. L. Infrared and Raman spectroscopic studies on iron oxide magnetic nano-particles and their surface modifications. *J. Magn. Magn. Mater.* **2012**, *324*, 1543−1550.
(49) Soler, M. A. G.; Qu, F. Chapter 14: Raman spectroscopy of iron oxide nanoparticles. In *Raman spectroscopy for nanomaterials characterization*; Challa, S. S. R. K ed., Springer-Verlag: Berlin Heidelberg 2012, 379−416, DOI: 10.1007/978-3-642-20620-7.
(50) Hanesch, M. Raman spectroscopy of iron oxides and (oxy)hydroxides at low laser power and possible applications in environmental magnetic studies. *Geophys. J. Int.* **2009**, *177*, 941−948.
(51) Volovšek, V.; Colombo, L.; Furić, K. Vibrational spectrum and normal coordinate calculations of the salicylic acid molecule. *J. Raman Spectrosc.* **1983**, *14*, 347−352.
(52) Kudin, K. N.; Ozbas, B.; Schniepp, H. C.; Prud'homme, R. K.; Aksay, I. A.; Car, R. Raman spectra of graphite oxide and functionalized graphene sheets. *Nano Lett.* **2008**, *8*, 36−41.
(53) Ferrari, A. C.; Robertson, J. Origin of the 1150 cm^{-1} Raman mode in nanocrystalline diamond. *Phys. Rev. B* **2001**, *63*, 121405.
(54) Ruiz-Medina, A.; Fernández-de Córdova, M. L.; Ortega-Barrales, P.; Molina-Díaz, A. Flow-through UV spectrophotometric sensor for determination of (acetyl)salicylic acid in pharmaceutical preparations. *Int. J. Pharm.* **2001**, *216*, 95−104.
(55) Wang, Y.; Xu, P.-P.; Li, X.-X.; Nie, K.; Tuo, M.-F.; Kong, B.; Chen, J. Monitoring the hydrolyzation of aspirin during the dissolution testing for aspirin delayed-release tablets with a fiber-optic dissolution system. *J. Pharm. Anal.* **2012**, *2*, 386−389.
(56) Wudarska, E.; Chrzescijanska, E.; Kusmierek, E. Electro-reduction of salicylic acid, acetylsalicylic acid and pharmaceutical products containing these compounds. *Port. Electrochim. Acta* **2014**, *32*, 295−302.
(57) Antonov, V. N.; Harmon, B. N.; Antropov, V. P.; Perlov, A. Y.; Yaresko, A. N. Electronic structure and magneto-optical Kerr effect of Fe_3O_4 and Mg^{2+}- or Al^{3+}-substituted Fe_3O_4. *Phys. Rev. B* **2001**, *64*, 134410.
(58) Yang, J. H.; Ramaraj, B.; Yoon, K. R. Preparation and characterization of superparamagnetic graphene oxide nanohybrids anchored with Fe_3O_4 nanoparticles. *J. Alloys Compd.* **2014**, *583*, 128−133.
(59) Aruoma, O. I.; Halliwell, B. The iron-binding and hydroxyl radical scavenging action of anti-inflammatory drugs. *Xenobiotica* **1988**, *18*, 459−470.
(60) Baltazar, M. T.; Dinis-Oliveira, R. J.; Duarte, J. A.; Bastos, M. L.; Carva, F. Antioxidant properties and associated mechanisms of salicylates. *Curr. Med. Chem.* **2011**, *18*, 3252−3264.
(61) Zhang, Z.; Su, T.; Han, Y.; Yang, Z.; Wei, J.; Jin, L.; Fan, H. A convergent synthetic platform for dual anticancer drugs functionalized by reduced graphene nanocomposite delivery for hepatocellular cancer. *Drug Delivery* **2021**, *28*, 1982−1994.
(62) Ruiz, O. N.; Fernando, K. A. S.; Wang, B.; Brown, N. A.; Luo, P. G.; McNamara, N. D.; Vangsness, M.; Sun, Y.-P.; Bunker, C. E. Graphene oxide: A nonspecific enhancer of cellular growth. *ACS Nano* **2011**, *5*, 8100−8107.
(63) Einafshar, E.; Asl, A. H.; Nia, A. H.; Mohammadi, M.; Malekzadeh, A.; Ramezani, M. New cyclodextrin-based nanocarriers for drug delivery and phototherapy using an irinotecan metabolite. *Carbohydr. Polym.* **2018**, *194*, 103−110.

https://doi.org/10.1021/acsbiomaterials.1c01603
ACS Biomater. Sci. Eng. XXXX, XXX, XXX−XXX